Mesoscale magnetic rings: complex magnetization reversal uncovered by FORC

G. Muscas[a,c,*], M. Menniti[a], R. Brucas[b], P. E. Jönsson[a]

[a]*Department of Physics and Astronomy, Uppsala University, Box 516, SE-751 20 Uppsala, Sweden*

[b]*Department of Engineering Sciences, Uppsala University, Box 534, SE-751 21 Uppsala, Sweden*

[c]*Department of Physics, University of Cagliari, I-09042 Monserrato, Italy*

*Corresponding author (e-mail address: giuseppe.muscas@dsf.unica.it)

Abstract

In this work, we investigate mesoscopic amorphous magnetic rings prepared by ion-implantation. The analysis is carried out combining conventional magnetization vs field measurements alongside MOKE microscopy imaging and, for the first time, first-order reversal curves (FORCs). With the information extracted from the FORC diagram, we can identify the presence of typical onion and vortex magnetic configurations, and also determine with high resolution the fields connected to their formation, stability, and annihilation. Furthermore, depending on the field and history, two different onion configurations exist, characterized by the presence of transverse or vortex domain walls. The FORC data reveals the different reversible/irreversible nature of the annihilation of the two onion configurations, and a signal peculiar of the presence of vortex domain walls. All these crucial information are not accessible with conventional M(H) loops, demonstrating that FORCs offer a unique perspective for the investigation of the physical phenomena of magnetic elements with complex geometries.

Keywords

Magnetic rings; onion state; magnetic vortex; magnetization reversal; FORC; amorphous magnets;

Highlights

- Mesoscale amorphous magnetic rings embedded in an amorphous matrix are investigated.
- The rings exhibit onion and vortex states analyzed by first-order reversal curves.
- First-order reversal curves discriminate between transverse and vortex domain walls of the onion state.
- First-order reversal curves capture unique details of the magnetization reversal.

Introduction

The investigation of small magnetic objects represents one of the most active fields in nanoscience. Thanks to advanced preparation processes, magnetic nanostructures can be tailored in both size and shape allowing to create controlled geometries [1–6] that manifest a multitude of peculiar spin configurations and physical effects, such as vortices, skyrmions, and chiral bubbles [7]. Such nanostructures find application in a wide range of fields, [1,8–10], with a special interest for magneto-recording [11,12].

A fundamental requisite to improve the density of magnetic memories is the presence of a stable remanence state. This state should be reached through a highly reproducible magnetization reversal process, and have negligible stray fields, to avoid dipolar coupling among adjacent elements that would affect the independent switching [13]. A vortex state, promoted by the curvature of simple geometries like disks, fulfills these conditions, except for the small stray field of the vortex core. The vortex core represents a highly energetic element, therefore, removing the core region by using a ring geometry vastly improves the stability of the vortex and minimizes stray fields [14]. The magnetization reversal of a ring is often characterized by two remanence states: as the field is reduced from saturation, the spins reorganize internally in a so-called "onion" configuration which is characterized by two parallel domains connected by 180º head-to-head and tail-to-tail domain walls. Reversing the field in the opposite direction induces the nucleation of a vortex in the entire ring, followed by the appearance of a second reversed onion at larger fields [15,16]. It is possible to distinguish onion configurations with transverse domain walls (T-onions) or with vortex domain walls (V-onions) [17], with the V-onions usually observed in wide microscale magnetic rings [15,18].

The formation and annihilation of onion and vortex states and, in general, the magnetization reversal inside rings can be controlled by engineering their geometry, i.e., by varying thickness and diameter [19], ring's symmetry [20], or by introducing additional elements like internal notches [21] or external connected nanowires [22]. Rings have proven to be a versatile platform for investigating emerging physical questions, such as the deterministic switching of the vortex chirality [23] or ultrafast magnetization dynamics [24]. At the same time, magnetic rings find application in several fields [10,25], in particular for ultra-high-density magnetic memories [14] and magneto-logic operations [26], exploiting the stability of their onion and vortex configurations. Moreover, rings can be easily combined in multi-ring structures, for even more advanced multi-state systems [27].

Since the multiple magnetic configurations of rings are related to a variety of different geometrical and structural factors, there comes the need of a comprehensive methodology of investigation of the field dependence of their magnetization reversal. In this respect, we investigate for the first time magnetic rings employing first-order reversal curves (FORCs). The FORC protocol allows identifying the presence of different magnetic states and their formation, stability, and annihilation as a function of the external field, with a much higher resolution compared to conventional magnetization vs field measurement. As a model system, we have studied mesoscopic elements consisting of ferromagnetic $Fe_{80}Zr_{10}B_{10}$ rings embedded in a paramagnetic $Fe_{89}Zr_{11}$ matrix. The mesoscopic size of the rings allows visualization of the magnetic domains through MOKE microscopy, corroborating the conclusions obtained from the FORC diagram.

Materials and Methods

The sample consists of a fully amorphous superstructure made of boron-implanted ring elements embedded in a $Fe_{89}Zr_{11}$ matrix. A 15 nm thick amorphous $Fe_{89}Zr_{11}$ film was deposited by magnetron sputtering on a Si (100) wafer covered by a 5 nm thick amorphous $Al_{70}Zr_{30}$ buffer layer to ensure amorphous growth, and with on top a 5 nm $Al_{70}Z_{r30}$ capping layer to protect the film from oxidation. Next, a Cr mask was deposited and holes reproducing rings were realized by employing a conventional photo-lithographic technique. The sample was doped by scanning the surface with a boron ion flux with an energy of 5 keV and an implantation dose of 2×10^{16} ions/cm^2, creating implanted regions reproducing the mask. Finally, the mask was removed by chemical etching, leaving a planar sample with $Fe_{80}Zr_{10}B_{10}$ elements embedded in the $Fe_{89}Zr_{11}$ matrix. The fabrication method is described in more details in ref. [28]. Doping with boron slightly expands the atomic Fe-Fe distances [29,30], enhancing the atomic exchange coupling [31] and hence increasing the Curie temperature (T_C) from 208 K in the original $Fe_{89}Zr_{11}$ matrix to 340 K in the implanted ring. At room temperature, the sample consists of the original paramagnetic (PM) matrix, with embedded soft ferromagnetic (FM) rings with ultra-low intrinsic magnetocrystalline anisotropy [28].

Magnetization vs field measurements were performed at room temperature in a longitudinal magneto-optical Kerr effect (L-MOKE) setup, which operates with p-polarized incident light. It was equipped with a Helmholtz coil to generate a field in the range ±7 mT, well above the saturation field of the rings, with a constant sweeping rate of 20 mT/s. A μ-metal shield reduced the background field to less than 0.002 mT. The laser spot extends over an area of about 7 mm^2. Considering the structure of the pattern, with an

area per ring of 1.6 10^{-3} mm^2, a single laser spot illuminates over 4000 rings at the same time. The measurement of each M(H) curve was repeated 100 times and then averaged to improve the signal-to-noise ratio.

First-order reversal curves (FORCs) were measured in the L-MOKE setup after degaussing the samples. Before a FORC measurement, the sample was saturated in a field of +7 mT, then the field was reduced down to the reversal field H_r, and an M(H_m) curve was recorded while scanning the measurement field H_m back up to saturation. The process was repeated 100 times, and then the data were averaged to improve the signal-to-noise ratio. The full set of M(H_m,H_r) curves were recorded by measuring as a function of reversal field in an interval from +0.50 to -2.00 mT, in steps of 0.01 mT. The FORC distribution (ρ-diagram) was obtained by computing the second-order mixed partial derivative of M with respect to H_m and H_r, normalized by the saturation magnetization M_S:

$$\rho(H_M, H_R) = -\frac{1}{2M_S}\frac{\partial^2 M(H_M,H_R)}{\partial H_M \partial H_R} \qquad (1)$$

The FORC distribution was calculated using a Matlab code implementing the FORCinel algorithm, which includes a locally-weighted regression smoothing algorithm [32]. For processing our data, we have used a smoothing factor (SF) of 8. Analyzing the FORC diagram can shed light on the complex magnetization reversal processes occurring in a sample. Depending on the H_r value, different starting magnetic configurations are created. Sweeping the measurement field H_m back to saturation reveals the reversal process of each individual configuration. Due to the double derivative, only progressive changes of the M(H_m, H_r) curves are visible in the ρ-diagram, hence only irreversible processes will be visualized. If a reversal event remains stable at the same H_m value while varying H_r, a positive signal will be visible in ρ only at the original H_r at which the specific reversal mechanism occurred for the first time. On the other hand, if a reversal event moves to a different H_m while changing H_r, a positive elongated ρ signal will extend to the new H_m value, and a tail-signal with negative values will mark the absence of the reversal process at the corresponding previous H_m position [33,34].

The magnetization reversal process during an M(H) loop was investigated also by recording real-time images of the magnetic domain structures with a commercial magneto-optical Kerr microscope and magnetometer (Evico magnetics) operating with Carl Zeiss optics with different magnifications (20X and 50X) at room temperature. The system was equipped with a low noise digital CCD camera and an

electromagnet. First, a degauss procedure was applied to bring all rings to the ground state configuration, which was a vortex for all elements investigated. Then, images of the magnetic domains were recorded during a hysteresis loop measured within a magnetic field range of ±7 mT. The images were recorded by averaging over 16 frames at each field step to reduce the noise. To maximize the magnetic contrast in the images, a background image of each sample was recorded before the measurements while applying an AC field, and then the images were collected using a real-time background subtraction mode. The images were processed using the software FIJI [35], normalizing the brightness to equalize the middle grey level for the paramagnetic background (matrix) in each image.

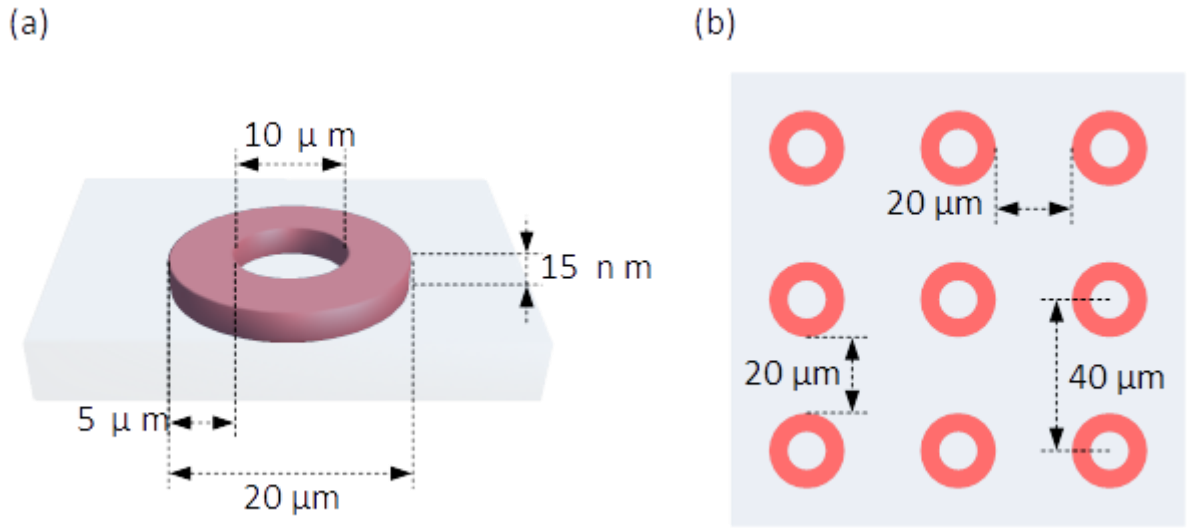

Figure 1. (a) Sketch of the rings prepared by ion implantation. (b) The pattern consists of a square lattice of regular rings of amorphous $Fe_{80}Zr_{10}B_{10}$ fully embedded in the original amorphous $Fe_{89}Zr_{11}$ matrix. The full pattern extends over an area of 5 X 5 mm. At room temperature, the matrix is paramagnetic while the boron implanted rings are ferromagnetic with ultra-low intrinsic anisotropy.

Results and Discussion

The sample consists of an amorphous composite structure with implanted regions with a ring shape. The rings have an internal/external diameter of 10/20 µm and thickness of 15 nm, and they are organized in a square lattice with a lattice constant of 40 µm, to minimize magnetostatic interactions among the elements (**figure 1**). The mesoscopic rings are embedded in the original amorphous matrix, with smooth interfaces, since no structural discontinuities exist between the two amorphous regions.

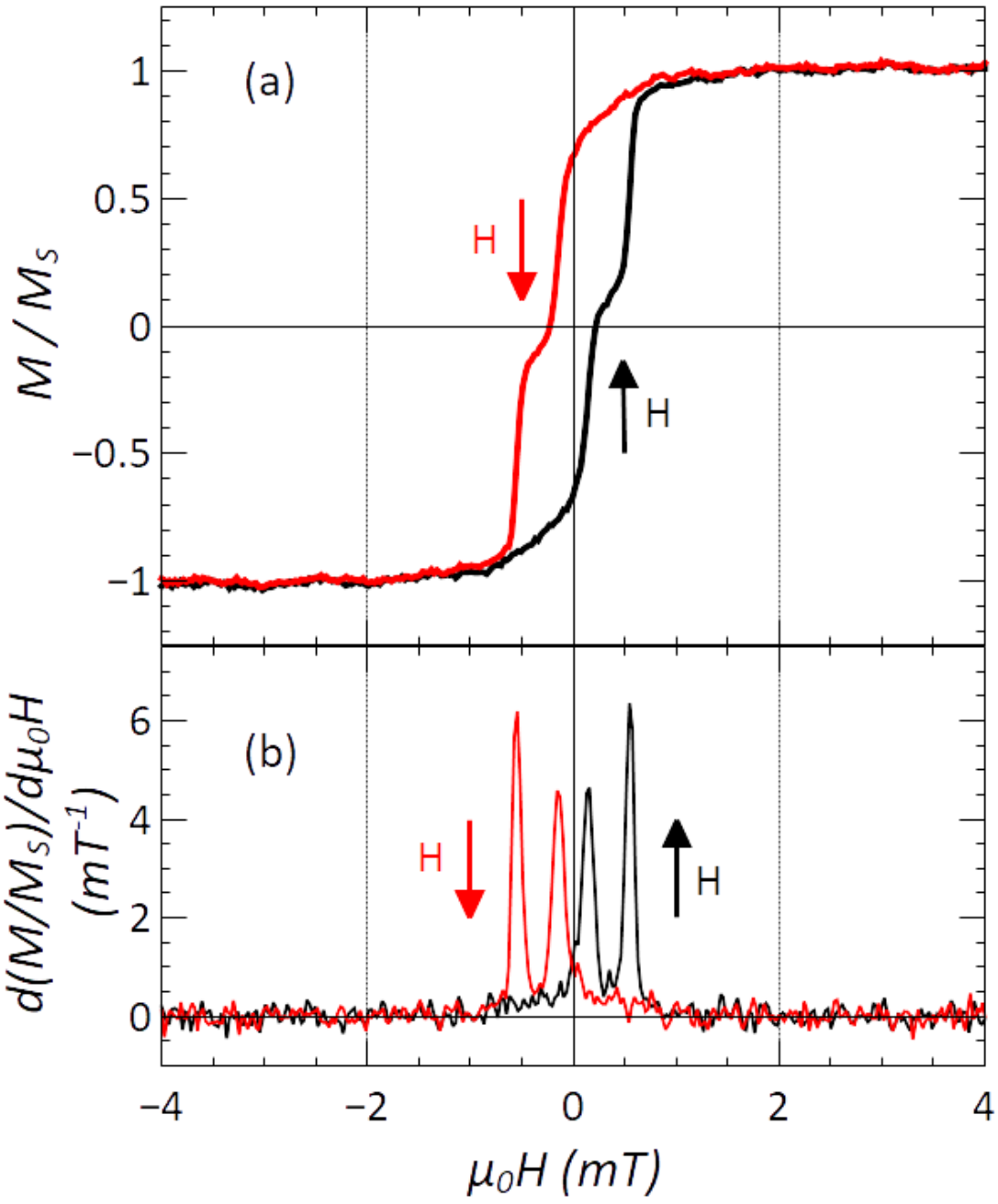

Figure 2. (a) Magnetization vs field curve and (b) the corresponding derivative measured at room temperature in an L-MOKE setup. The field sweep direction in each branch of the curves is distinguished by the black and red colors and illustrated by the corresponding arrows.

Figure 2a reports the M(H) curve of the rings showing a double step due to the formation of the onion and vortex magnetic configurations typical of ring structures [15]. The derivative curve of the hysteresis loop (**figure 2b**) evidences two peaks associated with the field responsible for the formation of onion and vortex configurations, at about 0.55 and 0.16 mT, respectively. The characteristic magnetic domain configurations observed measuring an equivalent loop with a MOKE microscope are shown in **figure 3**. At positive saturation, the magnetization is fully aligned parallel to the field, corresponding to the light homogeneous domain image of the rings shown in **figure 3a**. Reducing the field, the spins relax into an onion configuration with two large domains parallel to the field. They are connected by head-to-head and tail-to-tail domain walls, visible as darker grey regions due to the contrast of their curling magnetization (**figure 3b**) [18]. The onion configuration is stable at remanence (**figure 3c**) while reversing the field to small negative values induces a single vortex structure over the entire ring (**figure 3d-e**). Further increasing the negative field, the vortex is converted into a new onion state (**figure 3f-g**) [14], very close to the fully saturated condition (**figure 3h**).

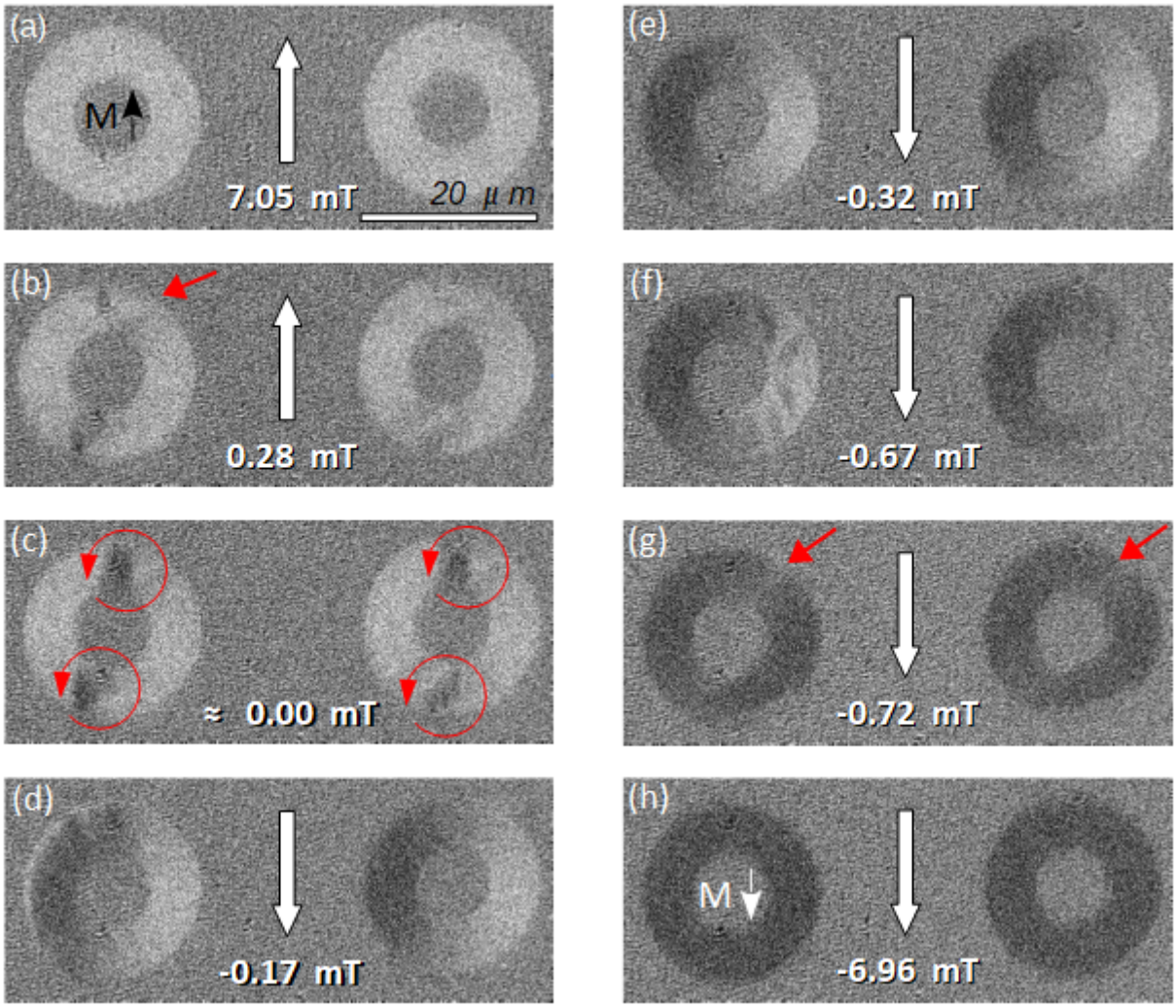

Figure 3. Kerr microscopy images of domain configurations in two of the magnetic rings as a function of the applied field, with its direction represented by the white bold arrow. The longitudinal configuration of the setup allows distinguishing the magneto-optical contrast of the magnetization component aligned to the field direction. The scan starts with positive saturation, i.e., magnetization M pointing up, which produces a light image of the rings (a). The progressive rotation of M while sweeping the field produces local darker shades of grey, up to reach full negative saturation with complete dark rings (h). The vortex domain walls in the onion configuration at remanence are evidenced by the curling red arrows (c). The small red arrows in panels (b) and (g) evidence areas with a different contrast compatible with transverse domain walls.

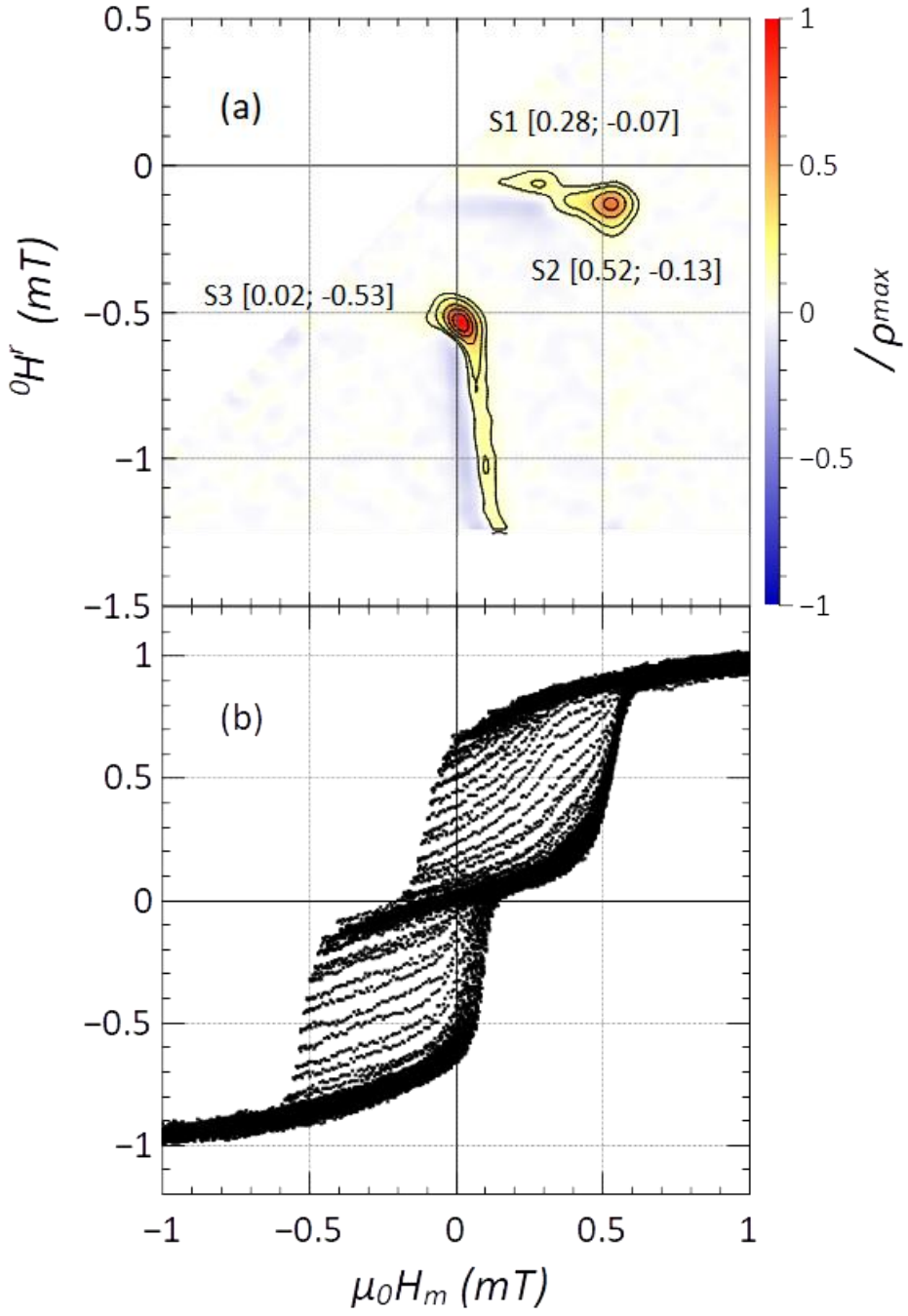

Figure 4. (a) FORC diagram calculated from (b) the first-order reversal curves measured at room temperature in an L-MOKE setup, using a smoothing factor SF = 8. For each main signal S, the field coordinates of the peak intensity are reported in square brackets.

The FORC diagram is reported in **figure 4**. For positive reversal fields, the FORC diagram does not exhibit any signal. MOKE images show the formation of the first onion configurations already for $\mu_0 H_r \approx 0.30$ mT (**figure 3b**). However, those onions exhibit structures with transverse walls or incomplete vortex walls [15,36]. Since the reversal process involving onions with transverse walls (T-onions) is not associated with any signal in the FORC diagram, one can conclude that the gradual annihilation of a transverse domain wall back into the starting saturated state is a fully reversible process. The signal in the FORC diagram appearing at the highest reversal field (S1) has an onion configuration with complete vortex walls as a starting configuration. The annihilation of a V-onion state is, therefore, a weak irreversible process, underlined by the corresponding very weak magnitude of S1. We note that the presence of V-onions configuration, can not be evidenced from conventional M(H) curves. Further reducing the reversal field, the starting configuration is a vortex inside the entire rings (**figure 3d**). Hence, the vortex annihilation is revealed by signal S2. The distribution of this signal in the reversal field range allows estimating the range of field associated with the nucleation process of the vortex. On the other hand, the corresponding measurement field range covered by S2 represents the extension of the annihilation field distribution of the same magnetic structure. The observation of several tens of rings by means of the MOKE microscope has evidenced that, for a given ring, the reversal is highly reproducible at the same field, within the resolution of the instrument, i.e., about 0.01 mT. On the other hand, different rings can show a small variation for the reversal fields. Since the laser spot illuminates over 4000 rings, the distribution of nucleation/annihilation fields of the ensemble of rings is easily captured by the FORC diagram. The vortex structure is stable for all reversal fields larger than those giving the signal S3. The starting domain structure connected to S3 is the reversed onion configuration, and the nucleation of vortices is, therefore, the process showing up in the FORC diagram as the signal S3. It appears as a positive ridge-like signal starting at $\mu_0 H_m \approx 0$ mT and extending up to $\mu_0 H_m \approx 0.15$ mT, leaving a clear negative signal tail in the diagram. At $\mu_0 H_r \approx -0.7$, the MOKE images show that the vortices are annihilated into almost saturated configurations, but with small regions with a weak variation of contrast (evidenced by arrows in **figure 3g**) compatible with a T-onion configuration. The FORC data reveal that the nucleation of the vortex from a T-onion requires a very small nucleation field. Reducing H_r, the T-onion becomes closer to saturation, and the nucleation field increases progressively, until $H_r \approx -1.2$ mT, when all onions collapse in a fully saturated structure. Then, sweeping back up the measurement field, we can expect to form first a T-onion, then converted in a V-onion without irreversible processes, finally followed by the nucleation of the vortex domain at higher H_m. A final interesting aspect emerging from

the FORC diagram is that the annihilation process of the vortices is not affected by the variation of its nucleation, indeed, the annihilation signal S2 does not show variation connected to the shift of the vortex nucleation signal S3. It is important to remark that all those fine aspects of the complex magnetization reversal of ring structures remain unexplored by a conventional examination of M(H) loops. In this framework, FORCs represent a powerful tool than can find application in the analysis of advanced geometries revealing the subtlest details of their magnetization reversal, such as the presence of stable and metastable magnetic configurations, and the range of field for their stability.

Conclusions

In this work, we have investigated the magnetization reversal of amorphous mesoscale magnetic rings combining the analysis of M(H) curve, magnetic domain images, and, for the first time, the FORC diagram. This analysis confirms the presence of the two typical metastable configurations of magnetic rings, i.e., the onion and the vortex states. The FORC diagram allows identifying their presence and the respective range of field stability. Furthermore, the diagram underlines the presence of transverse and vortex domain walls in the onion configurations. Indeed, only the annihilation of the onion configuration with vortex domain walls represents an irreversible process, which generates a specific signal in the FORC diagram. On the other hand, the hypothetical FORC diagram of a system where only onions with transverse walls are present should only exhibit signals connected to the nucleation and annihilation process of the full vortex state. From a more general point of view, the FORC diagram demonstrates its capabilities in identifying and quantifying magnetic phenomena with much higher sensitivity compared to conventional M(H) loops, discriminating between small variations of the same configuration. This makes FORCs a powerful tool for the study of magnetic elements with complex geometries, which are the object of strong interest for several technological applications.

Acknowledgments

The authors thank Gabriella Andersson for helping with the MOKE microscope.

Funding: This work was supported by the Swedish Research Council (VR) [grant number 2014-5951].

References

[1] Q. Gao, A. Zhao, Z. Gan, W. Tao, D. Li, M. Zhang, H. Guo, D. Wang, H. Sun, R. Mao, E. Liu, Facile fabrication and growth mechanism of 3D flower-like Fe3O4 nanostructures and their application as SERS substrates, CrystEngComm. 14 (2012) 4834. doi:10.1039/c2ce25198a.

[2] S. Alotaibi, J. Samba, S. Pokharel, Y. Lan, K. Uradu, A. Afolabi, I. Unlu, G. Basnet, K. Aslan, B.N. Flanders, A. Lisfi, B. Ozturk, Individually grown cobalt nanowires as magnetic force microscopy probes, Appl. Phys. Lett. 112 (2018) 092401. doi:10.1063/1.4997310.

[3] M.S. Saleh, C. Hu, R. Panat, Three-dimensional microarchitected materials and devices using nanoparticle assembly by pointwise spatial printing, Sci. Adv. 3 (2017) e1601986. doi:10.1126/sciadv.1601986.

[4] N. Bao, L. Shen, W. An, P. Padhan, C. Heath Turner, A. Gupta, Formation Mechanism and Shape Control of Monodisperse Magnetic CoFe 2 O 4 Nanocrystals, Chem. Mater. 21 (2009) 3458–3468. doi:10.1021/cm901033m.

[5] C. Phatak, Y. Liu, E.B. Gulsoy, D. Schmidt, E. Franke-Schubert, A. Petford-Long, Visualization of the Magnetic Structure of Sculpted Three-Dimensional Cobalt Nanospirals, Nano Lett. 14 (2014) 759–764. doi:10.1021/nl404071u.

[6] R. Liontas, J.R. Greer, 3D nano-architected metallic glass: Size effect suppresses catastrophic failure, Acta Mater. 133 (2017) 393–407. doi:10.1016/j.actamat.2017.05.019.

[7] A. Fernández-Pacheco, R. Streubel, O. Fruchart, R. Hertel, P. Fischer, R.P. Cowburn, Three-dimensional nanomagnetism, Nat. Commun. 8 (2017) 15756. doi:10.1038/ncomms15756.

[8] T. Mühl, J. Körner, S. Philippi, C.F. Reiche, A. Leonhardt, B. Büchner, Magnetic force microscopy sensors providing in-plane and perpendicular sensitivity, Appl. Phys. Lett. 101 (2012) 112401. doi:10.1063/1.4750058.

[9] P. Vavassori, M. Pancaldi, M.J. Perez-Roldan, A. Chuvilin, A. Berger, Remote Magnetomechanical Nanoactuation, Small. 12 (2016) 1013–1023. doi:10.1002/smll.201503351.

[10] X.L. Liu, Y. Yang, C.T. Ng, L.Y. Zhao, Y. Zhang, B.H. Bay, H.M. Fan, J. Ding, Magnetic Vortex Nanorings: A New Class of Hyperthermia Agent for Highly Efficient In Vivo Regression of Tumors, Adv. Mater. 27 (2015) 1939–1944. doi:10.1002/adma.201405036.

[11] S. Parkin, S.-H. Yang, Memory on the racetrack, Nat. Nanotechnol. 10 (2015) 195–198. doi:10.1038/nnano.2015.41.

[12] J.-G. Zhu, Y. Zheng, G.A. Prinz, Ultrahigh density vertical magnetoresistive random access memory (invited), J. Appl. Phys. 87 (2000) 6668–6673. doi:10.1063/1.372805.

[13] T.R. Albrecht, H. Arora, V. Ayanoor-Vitikkate, J.-M. Beaujour, D. Bedau, D. Berman, A.L. Bogdanov, Y.-A. Chapuis, J. Cushen, E.E. Dobisz, G. Doerk, He Gao, M. Grobis, B. Gurney, W. Hanson, O. Hellwig, T. Hirano, P.-O. Jubert, D. Kercher, J. Lille, Zuwei Liu, C.M. Mate, Y. Obukhov, K.C. Patel, K. Rubin, R. Ruiz, M. Schabes, Lei Wan, D. Weller, Tsai-Wei Wu, En Yang, Bit-Patterned Magnetic Recording: Theory, Media Fabrication, and Recording Performance, IEEE Trans. Magn. 51 (2015) 1–42. doi:10.1109/TMAG.2015.2397880.

[14] M. Kläui, C.A.F. Vaz, L. Lopez-Diaz, J.A.C. Bland, Vortex formation in narrow ferromagnetic rings, J. Phys. Condens. Matter. 15 (2003) R985–R1024. doi:10.1088/0953-8984/15/21/201.

[15] C.A.F. Vaz, T.J. Hayward, J. Llandro, F. Schackert, D. Morecroft, J.A.C. Bland, M. Kläui, M. Laufenberg, D. Backes, U. Rüdiger, F.J. Castaño, C.A. Ross, L.J. Heyderman, F. Nolting, A. Locatelli, G. Faini, S. Cherifi, W. Wernsdorfer, Ferromagnetic nanorings, J. Phys. Condens. Matter. 19 (2007) 255207. doi:10.1088/0953-8984/19/25/255207.

[16] Y.G. Yoo, M. Kläui, C.A.F. Vaz, L.J. Heyderman, J.A.C. Bland, Switching field phase diagram of Co nanoring magnets, Appl. Phys. Lett. 82 (2003) 2470–2472. doi:10.1063/1.1568167.

[17] M. Kläui, C.A.F. Vaz, J.A.C. Bland, L.J. Heyderman, F. Nolting, A. Pavlovska, E. Bauer, S. Cherifi, S. Heun, A. Locatelli, Head-to-head domain-wall phase diagram in mesoscopic ring magnets, Appl. Phys. Lett. 85 (2004) 5637–5639. doi:10.1063/1.1829800.

[18] M.H. Park, Y.K. Hong, B.C. Choi, M.J. Donahue, H. Han, S.H. Gee, Vortex head-to-head domain walls and their formation in onion-state ring elements, Phys. Rev. B. 73 (2006) 094424. doi:10.1103/PhysRevB.73.094424.

[19] J.J. Torres-Heredia, F. López-Urías, E. Muñoz-Sandoval, Micromagnetic simulation of iron nanorings, J. Magn. Magn. Mater. 294 (2005) e1–e5. doi:10.1016/j.jmmm.2005.03.043.

[20] K. Richter, A. Krone, M.-A. Mawass, B. Krüger, M. Weigand, H. Stoll, G. Schütz, M. Kläui, Localized domain wall nucleation dynamics in asymmetric ferromagnetic rings revealed by direct time-resolved magnetic imaging, Phys. Rev. B. 94 (2016) 024435. doi:10.1103/PhysRevB.94.024435.

[21] M. Kläui, C.A.F. Vaz, J.A.C. Bland, W. Wernsdorfer, G. Faini, E. Cambril, Domain wall pinning and controlled magnetic switching in narrow ferromagnetic ring structures with notches (invited), J. Appl. Phys. 93 (2003) 7885–7890. doi:10.1063/1.1557758.

[22] M. Lal, S. Sakshath, P.S.A. Kumar, Deterministic Switching of the Magnetization States in Cobalt Nanorings, IEEE Magn. Lett. 7 (2016) 1–5. doi:10.1109/LMAG.2016.2612167.

[23] R.P. Beardsley, S. Bowe, D.E. Parkes, C. Reardon, K.W. Edmonds, B.L. Gallagher, S.A. Cavill, A.W. Rushforth, Deterministic control of magnetic vortex wall chirality by electric field, Sci. Rep. 7 (2017) 7613. doi:10.1038/s41598-017-07944-9.

[24] J.-M. Hu, T. Yang, K. Momeni, X. Cheng, L. Chen, S. Lei, S. Zhang, S. Trolier-McKinstry, V. Gopalan, G.P. Carman, C.-W. Nan, L.-Q. Chen, Fast Magnetic Domain-Wall Motion in a Ring-Shaped Nanowire Driven by a Voltage, Nano Lett. 16 (2016) 2341–2348. doi:10.1021/acs.nanolett.5b05046.

[25] J. Llandro, T.J. Hayward, D. Morecroft, J.A.C. Bland, F.J. Castaño, I.A. Colin, C.A. Ross, Quantitative digital detection of magnetic beads using pseudo-spin-valve rings for multiplexed bioassays, Appl. Phys. Lett. 91 (2007) 203904. doi:10.1063/1.2813622.

[26] S.R. Bowden, U.J. Gibson, Optical Characterization of All-Magnetic NOT Gate Operation in Vortex Rings, IEEE Trans. Magn. 45 (2009) 5326–5332. doi:10.1109/TMAG.2009.2026573.

[27] F. López-Urías, J.J. Torres-Heredia, E. Muñoz-Sandoval, Cobalt double-ring and double-dot structures: Magnetic properties, Phys. B Condens. Matter. 483 (2016) 62–68. doi:10.1016/j.physb.2015.12.026.

[28] G. Muscas, R. Brucas, P.E. Jönsson, Bringing nanomagnetism to the mesoscale with artificial amorphous structures, Phys. Rev. B. 97 (2018) 174409. doi:10.1103/PhysRevB.97.174409.

[29] R. Moubah, A. Zamani, A. Olsson, S. Shi, A. Hallén, S. Carlson, D. Arvanitis, P. Nordblad, B. Hjörvarsson, P. Jönsson, Soft Room-Temperature Ferromagnetism of Carbon-Implanted Amorphous $Fe_{93}Zr_7$ Films, Appl. Phys. Express. 6 (2013) 053001. doi:10.7567/APEX.6.053001.

[30] J.M. Barandiaran, P. Gorria, J.C. Gomez Sal, L. Fernandez Barquin, S.N. Kaul, Influence of boron on the magnetic and transport properties of FeZr amorphous and nanocrystalline alloys, IEEE Trans. Magn. 30 (1994) 4776–4778. doi:10.1109/20.334218.

[31] K. a. Gallagher, M. a. Willard, V.N. Zabenkin, D.E. Laughlin, M.E. McHenry, Distributed exchange interactions and temperature dependent magnetization in amorphous $Fe_{88-x}Co_xZr_7B_4Cu_1$ alloys, J. Appl. Phys. 85 (1999) 5130–5132. doi:10.1063/1.369100.

[32] R.J. Harrison, J.M. Feinberg, FORCinel: An improved algorithm for calculating first-order reversal curve distributions using locally weighted regression smoothing, Geochemistry, Geophys. Geosystems. 9 (2008) n/a-n/a. doi:10.1029/2008GC001987.

[33] D.A. Gilbert, L. Ye, A. Varea, S. Agramunt-Puig, N. del Valle, C. Navau, J.F. López-Barbera, K.S. Buchanan, A. Hoffmann, A. Sánchez, J. Sort, K. Liu, J. Nogués, A new reversal mode in exchange coupled antiferromagnetic/ferromagnetic disks: distorted viscous vortex, Nanoscale. 7 (2015) 9878–9885. doi:10.1039/C5NR01856K.

[34] D.A. Gilbert, G.T. Zimanyi, R.K. Dumas, M. Winklhofer, A. Gomez, N. Eibagi, J.L. Vicent, K. Liu, Quantitative Decoding of Interactions in Tunable Nanomagnet Arrays Using First Order Reversal Curves, Sci. Rep. 4 (2015) 4204. doi:10.1038/srep04204.

[35] J. Schindelin, I. Arganda-Carreras, E. Frise, V. Kaynig, M. Longair, T. Pietzsch, S. Preibisch, C. Rueden, S. Saalfeld, B. Schmid, J.-Y. Tinevez, D.J. White, V. Hartenstein, K. Eliceiri, P. Tomancak, A. Cardona, Fiji: an open-source platform for biological-image analysis, Nat. Methods. 9 (2012) 676–682. doi:10.1038/nmeth.2019.

[36] R.D. McMichael, M.J. Donahue, Head to head domain wall structures in thin magnetic strips, IEEE Trans. Magn. 33 (1997) 4167–4169. doi:10.1109/20.619698.